

# Density-driven submerged granular flows in rotating drums

Yu Chen<sup>1,\*</sup> and Yixiang Gan<sup>1,\*\*</sup>

<sup>1</sup>School of Civil Engineering, The University of Sydney, Sydney, Australia

**Abstract.** Granular flows and segregation phenomena play critical roles in diverse natural and industrial processes. We investigated the dynamics of mono-dispersed and binary granular mixtures in submerged rotating drums using combined experimental and numerical methods. Mono-dispersed granular flows demonstrate clear transitions between rolling and cascading regimes, strongly influenced by particle density, fluid properties, and rotation speeds; these transitions are effectively captured by a modified Froude number ( $Fr^*$ ) incorporating particle-fluid density differences. Extending this analysis to binary mixtures reveals a density-driven segregation mechanism, with the mixing index exhibiting an exponential relationship with the effective density ratio ( $\mathcal{D}$ ). Our findings offer enhanced fundamental understanding of submerged granular flows and segregation dynamics, providing valuable insights for both scientific exploration and engineering practices.

## 1 Introduction

Granular materials, composed of discrete solid particles varying in size, shape, and density, are commonly dispersed in ambient fluids. Driven primarily by gravity, such systems are prevalent in natural phenomena such as snow avalanches, landslides, and debris flows [1]. In particular, granular segregation, the spontaneous separation due to particle differences, significantly impacts processes ranging from sediment transport to pharmaceutical manufacturing and wood pulp engineering [2, 3]. Therefore, accurately predicting granular flow, including segregation behaviour under different conditions, is essential for both scientific understanding and practical applications.

Extensive research has focused on mono-dispersed granular flow dynamics in rotating drums, highlighting significant influences from particle properties [4, 5]. Within these drums, granular flow typically develops as a moving surface layer overlaying a relatively static, densely packed bed [6]. Increasing rotation speed sequentially triggers different flow regimes: sliding, surging, slumping, rolling, cascading, cataracting, and centrifuging, each characterised by unique flow dynamics and particle interactions [7]. Of these regimes, the rolling and cascading states are particularly relevant, marked respectively by steady-state particle circulation and dilute, collision-dominated interactions [8]. To characterise these complex behaviours, the dimensionless parameter, such as the Froude number ( $Fr = \sqrt{\omega^2 R/g}$ ), captures the interplay between gravitational, inertial, and buoyancy forces [9]. Parallel investigations into binary granular mixtures reveal even more intricate phenomena, especially granular segregation, where particles spontaneously separate due to den-

sity differences, forming distinct "central core" structures under dry conditions [10].

Submerged granular flows exhibit considerable complexity owing to viscous interactions between particles and ambient fluids. While granular dynamics in low-density fluids (*e.g.*, air) are predominantly governed by particle-particle collisions and gravitational forces [11, 12], complexities escalate significantly when particle and fluid densities become comparable, leading to distinct buoyancy effects. To characterise these density-driven phenomena, the dimensionless buoyancy parameter ( $\Delta\rho/\rho_s = (\rho_s - \rho_f)/\rho_s$ ) has proven effective in differentiating submerged granular behaviours from their dry counterparts [13]. Moreover, previous studies have demonstrated the critical influence of grain-fluid density ratios in identifying distinct flow regimes and segregation dynamics within immersed granular media [14]. Experimental investigations of chute flows and rotating drum configurations further underscore the significant role that fluid properties, particle characteristics, and rotation speed play in determining granular flow morphologies and dynamics [15].

To gain a deeper understanding of the effects of particle density in submerged rotating drum systems, this study uses a combined experimental and numerical approach to systematically investigate both granular flow and segregation. By introducing and validating a modified Froude number to characterise mono-dispersed flows, and employing a mixing index to quantify segregation efficiency in binary mixtures, the analysis highlights critical parameters governing granular behaviour.

## 2 Methods

### 2.1 Experimental setup and configuration

The experiments were conducted using rotating drum setups illustrated in Fig. 1(a). A cylindrical drum fabricated

\*e-mail: [yu.chen2@sydney.edu.au](mailto:yu.chen2@sydney.edu.au)

\*\*e-mail: [yixiang.gan@sydney.edu.au](mailto:yixiang.gan@sydney.edu.au)

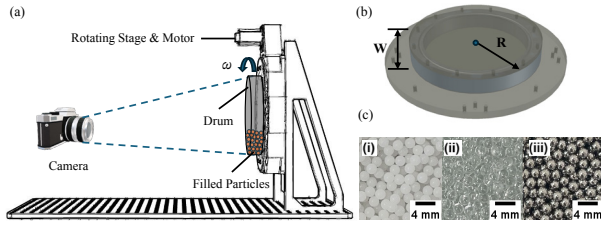


**Figure 1.** Experimental methods: Schematic of (a) experimental setup and apparatus, (b) the cylindrical acrylic drum with thickness  $W = 30$  mm and radius  $R = 75$  mm. (c) The three particle types used in studies: from left to right, polyoxymethylene (POM,  $\rho_s = 1382$  kg/m<sup>3</sup>), glass beads ( $\rho_s = 2363$  kg/m<sup>3</sup>) and stainless steel ( $\rho_s = 7803$  kg/m<sup>3</sup>).

from transparent acrylic was used, shown in Fig.1(b), with inner radius ( $R$ ) of 75 mm and axial lengths of 30 mm. The rotation was driven by motorised stages, offering precise speed control in the range of  $\omega \in [5, 60]$  rpm, covering both rolling and cascading regimes critical for practical and scientific interests. The drum was fully immersed in purified water (density  $\rho_w = 1000$  kg/m<sup>3</sup> and viscosity  $\eta_w = 0.001$  Pa · s).

Experiments were conducted using mono-sized spherical particles, shown in Fig. 1(c), of polyoxymethylene (POM,  $\rho_s = 1382$  kg/m<sup>3</sup>), glass beads ( $\rho_s = 2363$  kg/m<sup>3</sup>), and stainless steel ( $\rho_s = 7803$  kg/m<sup>3</sup>), all with a nominal diameter of  $2$  mm  $\pm$  3%. Two experimental configurations were employed: mono-dispersed and binary mixtures. Mono-dispersed tests maintained a filling ratio of approximately 25 %, while binary mixtures consisted of equal numbers of two particle types ( $\sim 14,270$  particles each), yielding a filling ratio of 35.6 %. Particle dynamics and flow patterns were recorded using a high-speed camera, and granular velocities were extracted through Particle Image Velocimetry (PIV) analyses [16]. Experimental repeatability was confirmed, with measured angles of repose exhibiting standard deviations below 5 %.

## 2.2 Numerical simulations

Numerical simulations were performed using two distinct approaches to address both mono-dispersed and binary granular flow scenarios. For mono-dispersed granular flows, a two-phase Eulerian CFD model coupled with the  $\mu(I)$  rheology was adopted, treating both fluid and solid phases as continuous, interpenetrating media. The computational domain replicated the experimental drum geometry, and mesh sensitivity analysis confirmed that a mesh size of  $\ell/R = 1/37.5$  provided an optimal balance between accuracy and computational efficiency.

The drag force governing fluid-particle interactions was modeled using the Gidaspow drag formulation [17]. The apparent viscosity of the solid phase was described by the  $\mu(I)$  rheology model, expressed as  $\mu(I) = \mu_s + (\mu_d - \mu_s)/(I_0/I + 1)$ , where  $I_0$  is an empirically determined reference value. The friction coefficients  $\mu_s$  and  $\mu_d$ , representing the static and dynamic limits, were experimentally obtained by measuring the "start" and "stop" angles

in preliminary tests, with  $\mu_d = \tan \theta_{start}$  and  $\mu_s = \tan \theta_{stop}$  [18]. The inertial number,  $I$ , is defined as  $I = \dot{\gamma} d_s / \sqrt{p_s / \rho_s}$ , where  $\dot{\gamma}$  denotes the shear rate,  $d_s$  is the particle diameter, and  $p_s$  is the solid pressure.

For binary granular mixtures, an unresolved CFD-DEM model [19] was adopted, which averages fluid quantities over volumes larger than individual particles. However, the limitation lies in the small-scale hydrodynamic features near particle surfaces, such as boundary layers and interstitial vortices, which are not resolved in this approach. The fluid phase was modelled using Eulerian-averaged Navier–Stokes equations, while particle dynamics was governed by the discrete element method (DEM) with the Hertz contact model. The CFD mesh size was set at twice the particle diameter ( $2d_s$ ), with a DEM time step of  $10^{-4}$  s and a CFD time step of  $10^{-3}$  s. Simulations also explored a range of fluid and particle densities by varying the fluid density  $\rho_f \in [0.2\rho_w, \rho_w]$  and particle density  $\rho_s \in [1.400\rho_w, 9.743\rho_w]$ . In addition, the lubrication forces are not considered, as their effect is negligible when the dimensionless ratio  $I/J = \sqrt{\rho_s P_s} \cdot d_s / \eta_f$  is large, where  $P_s$  represents the confining pressure. In our system,  $I/J \approx 5,000$  even at the lowest  $\omega = 5$  rpm, indicating lubrication dissipation is minimal [20]. The segregation between binary mixtures is quantified by the Lacey mixing index  $M = (\sigma^2 - \sigma_0^2) / (\sigma_m^2 - \sigma_0^2) \in [0, 1]$ , with  $\sigma^2 = \sum_{i=1}^N (\phi_i - \phi_m)^2 / (N - 1)$ . Here,  $N$  denotes the total number of equal-sized cells that collectively contain all grains. The local concentration of tracer grains in the  $i$ -th cell is  $\phi_i$ , and  $\phi_m$  represents the mean concentration over all cells. The theoretical maximum variance is given by  $\sigma_0^2 = \phi_m \cdot (1 - \phi_m)$ , while the minimum variance corresponding to  $\sigma_m^2 = \sigma_0^2 / n$ , where  $n$  is the number of grains in each cell [21].

To quantify the agreement between numerical and experimental results, the standard deviation of the error,  $\sigma_e$ , was calculated. For mono-dispersed cases,  $\sigma_e$  of the dynamic angle of repose is 2.3%, while for binary mixtures,  $\sigma_e$  of the mixing index remains under 3%. These results confirm the reliability of the simulation framework.

## 3 Results

### 3.1 Flow patterns and shear rate

In the mono-dispersed granular flow, as illustrated in Fig. 2, the flow regimes are classified based on surface morphology. The lighter particles (POM) exhibit cascading behaviour (S-shaped surface) across the entire range of angular velocities ( $\omega = 5$ –20 rpm). In contrast, the heavier particles (glass beads and stainless steel) maintain rolling behaviour (flat surface) at  $\omega = 5$  rpm before transitioning to cascading at higher angular velocities ( $\omega \geq 10$  rpm). Increasing  $\omega$  also results in elevated shear rates, as higher rotational speeds inject greater kinetic energy, intensifying particle interactions. Moreover, particle density significantly influences shear rate magnitudes, with heavier particles exhibiting higher shear rates due to enhanced inertial and gravitational effects.

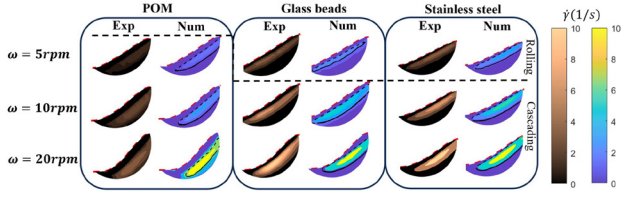


**Figure 2.** Shear rate distributions in submerged mono-dispersed granular systems for (left to right) POM particles, glass beads, and stainless steel particles, showing comparison between experimental measurements and numerical simulations. Dashed lines delineate rolling and cascading flow regimes. The granular flow surface is indicated by red dashed lines, while black solid lines mark the flow region interface.

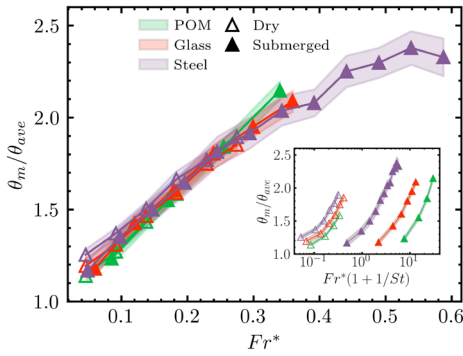


**Figure 3.** Correlation between the flowing surface profile and the modified Froude number ( $Fr^*$ ) based on experimental data, with the normalised dynamic angle of repose expressed as  $\theta_m/\theta_{ave}$ , where  $\theta_{ave} = \tan^{-1}[(\mu_s + \mu_d)/2]$ , and the Stokes number defined as  $St = d^{1.5} \sqrt{\Delta\rho g \rho_s} / (18\eta_f)$ .

### 3.2 Dynamic angle of repose

The dynamic angle of repose ( $\theta_m$ ), defined as the maximum inclination angle of the granular free surface at steady state, increased with rotational speed ( $\omega$ ) and fluid density. To systematically quantify the combined influences of inertial and buoyancy forces, a modified Froude number was introduced as  $Fr^* = \sqrt{\rho_s \omega^2 R / g(\rho_s - \rho_f)}$ . It shares dimensional similarities with the inverse of the Euler number  $Eu^{-1} = \rho_f U^2 / \Delta p$ , a parameter commonly used to characterise energy losses in internal flows, where  $U$  is the characteristic velocity of the flow and  $\Delta p$  represents the pressure drop. In addition,  $Fr^*$  incorporates the dimensionless buoyancy-corrected parameter  $\Delta\rho/\rho_s = (\rho_s - \rho_f)/\rho_s$ , valid for  $\rho_s > \rho_f$ , and reduces to the traditional Froude number  $Fr = \sqrt{(\omega^2 R / g)}$  in the dry limit as  $\rho_f/\rho_s \rightarrow 0$ , which is analogous to buoyancy-corrected inertial numbers proposed for submerged granular heap flows, where particle dynamics are governed by their apparent weight [14]. As shown in Fig. 3,  $Fr^*$  is universally correlated with the observed variations in  $\theta_m$  across different particle and fluid properties. Additionally, to account for frictional variations,  $\theta_m$  was normalised by an averaged friction angle,  $\theta_{ave} = \tan^{-1}[(\mu_s + \mu_d)/2]$ , representing both static and dynamic friction characteristics of the particles. The inset of Fig. 3 shows that the normalised

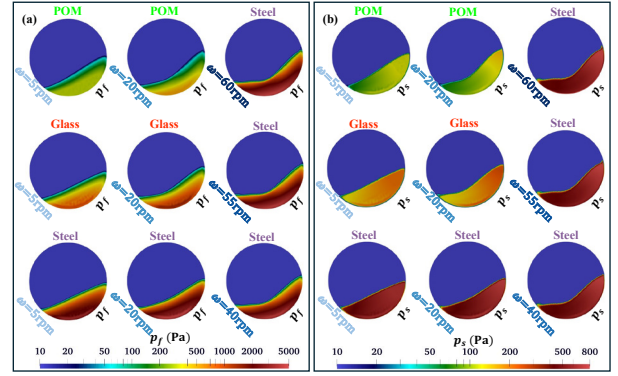


**Figure 4.** Predicted pressure distributions under submerged conditions for different materials at varying rotation speeds: (a) pore fluid pressure and (b) solid pressure.

dynamic angle  $\theta_m/\theta_{ave}$  increases with  $Fr^*(1 + 1/St)$  both dry and submerged flows. The scaling, proposed by the previous study [9], was shown to unify results across grain types and drum geometries in dry systems. Our findings confirm this trend in dry flows, but the scaling diminishes when fluid effects become significant.

### 3.3 Pressure distribution

Numerical simulations provide detailed measurements of solid pressure ( $p_s$ ) and pore fluid pressure ( $p_f$ ) distributions in submerged granular flows, which are obtained after the granular system reaches steady state and are spatially averaged over time. As shown in Fig. 4, both  $p_s$  and  $p_f$  increased with particle density, while  $\omega$  had a limited effect at medium and high densities. In addition,  $p_f$  was significantly higher than  $p_s$ , indicating the dominant influence of pore fluid pressure in submerged granular flows.

### 3.4 Granular segregation in binary mixtures

Extending from mono-dispersed granular flow to binary mixtures, granular segregation phenomena were systematically examined through the mixing index ( $M$ ) and the effective density ratio ( $\mathcal{D}$ ). The relationship between segregation efficiency and  $\mathcal{D}$  is illustrated in Fig. 5(a). Results indicate that  $M$  decreases exponentially with increasing  $\mathcal{D}$ , following the relation  $M = (1 - c)e^{b(\mathcal{D}-1)} + c$ , where fitting parameters  $b < 0$  and  $0 < c < 1$ . In the case where  $\rho_h = \rho_l$ , the mixture becomes mono-disperse, yielding  $(\mathcal{D}, M) = (1, 1)$ . Conversely, as the density of the light particles approaches that of the surrounding fluid ( $\rho_l \rightarrow \rho_f$ ), the buoyancy force becomes dominant, leading to an infinite effective density ratio and a fully segregated state where  $M \rightarrow c$ . The parameter  $c$  thus characterises the maximum segregation achievable under the given system conditions, which could be governed by the drum geometry, rotation speed, and filling state. Furthermore, parameters  $b$  and  $c$  evolve distinctly with the global Reynolds number ( $Re = \rho_f \omega R d_p / \eta_f$ ), where  $c$  exhibits a logarithmic linearity, while  $b$  displays a bilinear behaviour, suggesting a regime transition from viscous to inertial domi-

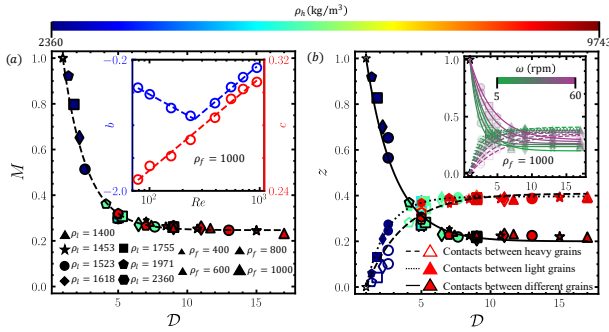


**Figure 5.** (a) Mixing index  $M$  as a function for the effective density ratio  $\mathcal{D}$  at  $\omega = 5$  rpm. Dashed lines indicate the fitted functions, and the hollow pentagram denotes  $(\mathcal{D}, M) = (1, 1)$ . The inset illustrates the parameters,  $b$  and  $c$  vs.  $Re$ . (b) The contact number ratio,  $z$ , plotted against  $\mathcal{D}$  at  $\omega = 5$  rpm. The upper hollow pentagram is for  $(\mathcal{D}, z) = (1, 1)$ , while the bottom hollow pentagram is for  $(\mathcal{D}, z) = (1, 0)$ . The inset is for  $z$  versus  $\mathcal{D}$  for various rotating speeds.

nance. In submerged binary mixtures, segregation arises not only from gravitational settling but also from fluid-mediated forces. The heavy particle cluster experiences a net force from buoyancy and drag aligned with the flow, shifting it in the direction of drum rotation. As  $\omega$  increases, the enhanced drag facilitates the outward migration of heavy grains. At the high  $\mathcal{D}$  regime, light particles behave similarly to the fluid, allowing heavy particles to decouple and segregate more effectively.

Further insights from particle-scale simulations (Fig. 5(b)) reveal the proportion of three contact types—heavy-heavy ( $z_h$ ), light-light ( $z_l$ ), and different particle contacts ( $z_d$ ). All three types follow exponential trends with varying  $\mathcal{D}$ , mirroring the behaviour of  $M$ . At  $\mathcal{D} = 1$ , the system exhibits ideal mixing with  $z_d = 1$  and  $z_h = z_l = 0$ . Increasing  $\mathcal{D}$  promotes segregation, raising  $z_h$  and  $z_l$  but diminishing  $z_d$ . Additionally, higher  $\omega$  expand the contact interface between segregated heavy clusters and surrounding lighter particles, increasing  $z_d$  while correspondingly decreasing  $z_h$  and  $z_l$ .

## 4 Conclusion

This study investigates the flow dynamics and segregation behaviours of mono-dispersed and binary granular materials in submerged rotating drums through integrated experimental and numerical analyses. Results demonstrate a clear transition in granular flow regimes from rolling to cascading with effects of both particle density and rotating speed. A modified Froude number ( $Fr^*$ ), incorporating particle-fluid density differences, captures these flow regime transitions and correlates with dynamic angles of repose across various particle properties and fluid conditions. Numerical simulations also highlight that pore fluid pressures dominate significantly over solid pressures under submerged conditions. In the binary mixtures, a new dimensionless number,  $\mathcal{D}$ , is introduced to link grain-fluid properties directly to the macroscopic mixing index,  $M$ .

Furthermore, we propose a new predictive model for  $M$  in density-driven segregation systems, capable of characterising the evolution of segregation from a well-mixed to a nearly segregated state. Collectively, these findings provide fundamental insights into submerged granular flows, offering practical implications for optimising industrial material handling and processing and improving our understanding of fluid-mediated granular mechanics.

## References

- [1] T. Takahashi, *Journal of the Hydraulics Division* **104**, 1153 (1978).
- [2] B. Ferdowsi, C.P. Ortiz, M. Houssais, D.J. Jerolmack, *Nature communications* **8**, 1363 (2017).
- [3] S. Badar, I.H. Farooqi, *Environmental protection strategies for sustainable development* pp. 397–436 (2012).
- [4] T. Yao, H. Yang, S.D.N. Lourenço, B.A. Baudet, F.C.Y. Kwok, *Engineering Geology* **303** (2022).
- [5] S.B. Savage, M. Babaei, T. Dabros, *Mechanics Research Communications* **56**, 1 (2014).
- [6] G.D.R. MiDi, *Eur Phys J E Soft Matter* **14**, 341 (2004).
- [7] M. Dong, Z. Wang, B. Marks, Y. Chen, Y. Gan, *Physics of Fluids* **35** (2023).
- [8] G. Félix, V. Falk, U. d’Ortona, *The European Physical Journal E* **22**, 25 (2007).
- [9] F. Pignatelli, C. Asselin, L. Krieger, I.C. Christov, J.M. Ottino, R.M. Lueptow, *Phys Rev E Stat Nonlin Soft Matter Phys* **86**, 011304 (2012).
- [10] D. Khakhar, A.V. Orpe, S. Hajra, *Physica A: Statistical Mechanics and its Applications* **318**, 129 (2003).
- [11] C.H. Lee, Z. Huang, *Advances in Water Resources* **115**, 286 (2018).
- [12] G.G. Zhou, K.F. Cui, L. Jing, T. Zhao, D. Song, Y. Huang, *Journal of Geophysical Research: Solid Earth* **125**, e2020JB019536 (2020).
- [13] G. Juarez, P. Chen, R.M. Lueptow, *New Journal of Physics* **13**, 053055 (2011).
- [14] C. Cassar, M. Nicolas, O. Pouliquen, *Physics of Fluids* **17** (2005).
- [15] Y. Chen, S. Suo, M. Dong, H. Zhong, D. Wei, Y. Gan, *Physics of Fluids* **36** (2024).
- [16] A. Medina, J. Cordova, E. Luna, C. Trevino, *Physics Letters A* **250**, 111 (1998).
- [17] D. Gidaspow, *Multiphase Flow and Fluidization: Continuum and Kinetic Theory Descriptions* (Academic press, 1994)
- [18] Y. Forterre, O. Pouliquen, *Annu. Rev. Fluid Mech.* **40**, 1 (2008).
- [19] Y. Tsuji, T. Kawaguchi, T. Tanaka, *Powder technology* **77**, 79 (1993).
- [20] M. Trulsson, B. Andreotti, P. Claudin, *Physical review letters* **109**, 118305 (2012).
- [21] P.M.C. Lacey, *Journal of applied chemistry* **4**, 257 (1954).